

HYSTERESIS IN LAYERED SPRING MAGNETS

J. SAMUEL JIANG

Materials Science Division
Argonne National Laboratory
Argonne, IL 60439

HANS G. KAPER

Mathematics and Computer Science Division
Argonne National Laboratory
Argonne, IL 60439

GARY K. LEAF

Mathematics and Computer Science Division
Argonne National Laboratory
Argonne, IL 60439

(Communicated by Shouhong Wang)

ABSTRACT. This article addresses a problem of micromagnetics: the reversal of magnetic moments in layered spring magnets. A one-dimensional model is used of a film consisting of several atomic layers of a soft material on top of several atomic layers of a hard material. Each atomic layer is taken to be uniformly magnetized, and spatial inhomogeneities within an atomic layer are neglected. The state of such a system is described by a chain of magnetic spin vectors. Each spin vector behaves like a spinning top driven locally by the effective magnetic field and subject to damping (Landau–Lifshitz–Gilbert equation). A numerical integration scheme for the LLG equation is presented that is unconditionally stable and preserves the magnitude of the magnetization vector at all times. The results of numerical investigations for a bilayer in a rotating in-plane magnetic field show hysteresis with a basic period of 2π at moderate fields and hysteresis with a basic period of π at strong fields.

1. Introduction. Exchange-spring coupled magnets (*spring magnets*, for short) hold significant promise for applications in information recording and storage devices. Spring magnets consist of nanodispersed hard and soft magnetic phases that are coupled at the interfaces. (In a hard material, the magnetic moment tends to be aligned with the easy axis; in a soft material, it is more or less free to align itself with the local magnetic field.) The superior magnetic properties of a spring magnet stem from the fact that the soft phase enhances the magnetization of the composite [1, 2, 3, 4, 5, 6]. Since the performance of a spring magnet is determined by the stability of the soft phase against magnetization reversal, it is important to identify the factors affecting the reversal process.

Thin films provide an interesting class of simple models for which one can perform both physical and computational experiments. A spring-magnet structure can be

1991 *Mathematics Subject Classification.* 34C23, 49S05, 58C07, 82D40.

Key words and phrases. Micromagnetics, spring magnets, hysteresis, Landau–Lifshitz–Gilbert equation.

realized by interleaving hard and soft magnetic layers, and because the magnetic properties vary predominantly along the normal direction, the structure of such spring magnets is essentially one dimensional.

In this article we investigate magnetic reversal in a hard/soft bilayer—a layer of soft material on top of a layer of hard material—with strong coupling at the interface. The hard and soft layers both consist of several atomic layers; each atomic layer is treated as uniformly magnetized, and spatial inhomogeneities within an atomic layer are neglected. The state of the bilayer is thus described by a chain of spins, each spin representing the magnetic moment of an atomic layer.

The dynamics of a magnetic moment are entirely local. A magnetic moment is like a spinning top, which is driven by the effective magnetic field and subject to damping. The relevant equation was first formulated by Landau and Lifshitz [7] and later given in an equivalent form by Gilbert [8]. The local effective field is derived variationally from an energy functional [9].

The Landau–Lifshitz–Gilbert equation preserves the magnitude of the magnetic moment, and it is important to maintain this property in numerical approximations. Our first purpose in this article is to present an integration scheme that conserves magnetization at all times.

Our second purpose is to present some results of numerical simulations for a bilayer. They show two types of rotational hysteresis: one at moderate fields with a basic period of 2π , which is associated with the irreversible behavior of the chirality (“handedness”) of the chain of magnetic spins in the soft layers; another at strong fields with a basic period of π , which is associated with the irreversible behavior of a full-length transition of the chain of magnetic spins in both the hard and the soft layers. These results explain the experimental observation of hysteresis in some torque measurements [10]. They also agree qualitatively with some magneto-optical measurements of the magnetization angle [11]. However, they differ at the quantitative level. The discrepancy is due to the one-dimensional model, which does not allow for the nucleation and motion of nanodomains.

The remainder of this article consists of three sections. In Section 2, we describe the mathematical model, together with the numerical approximation procedure. In Section 3, we present some simulation results for hard/soft bilayers. (Additional results are presented in [12].) In Section 4, we summarize our conclusions.

2. Mathematical model. A layered spring magnet is a multilayer structure, which consists of N_h atomic layers of a hard magnetic material adjacent to N_s atomic layers of a soft magnetic material,

$$\begin{aligned} \text{Hard layers :} \quad & i \in I_h = \{1, \dots, N_h\}, \\ \text{Soft layers :} \quad & i \in I_s = \{N_h + 1, \dots, N_h + N_s\}. \end{aligned}$$

We put $I = I_h \cup I_s$ and $N = N_h + N_s$. The atomic layers are homogeneous, and variations occur only in the direction normal to the layers. We assume for convenience that the atomic layers are equally thick; their thickness d is of the order of angstroms ($1 \text{ \AA} = 1.0 \cdot 10^{-8} \text{ cm}$).

We adopt a right-handed Cartesian (x, y, z) coordinate system, where the x and y axes are in the plane of an atomic layer, the x axis coincides with the easy axis of the hard material, and the z axis is in the direction normal to the layers; \mathbf{e}_x , \mathbf{e}_y , and \mathbf{e}_z are the unit vectors in the direction of increasing x , y , and z , respectively. In a polar (ϕ, θ) coordinate system, ϕ is the out-of-plane angle and θ the in-plane angle measured counterclockwise from the positive x axis.

The state of the bilayer is completely described by the set of *magnetic moments*,

$$\mathbf{M} = \{\mathbf{M}_i : i \in I\}. \quad (1)$$

Each \mathbf{M}_i is a vector-valued function of time t , with components $M_{i,x}$, $M_{i,y}$, and $M_{i,z}$. The magnitude M_i of \mathbf{M}_i is the *magnetization*, the unit vector $\mathbf{m}_i = \mathbf{M}_i/M_i$ is the *magnetic spin* in the i th layer. The magnetization is constant at all times and equal to the local saturation magnetization,

$$\mathbf{M}_i(t) = M_i \mathbf{m}_i(t), \quad \text{with } M_i = \begin{cases} M_h & \text{if } i \in I_h, \\ M_s & \text{if } i \in I_s. \end{cases} \quad (2)$$

Here, M_h and M_s are the values of the saturation magnetization for the hard and soft material, respectively. Each magnetic spin can be specified in terms of its Cartesian or polar components,

$$\mathbf{m}_i = (m_{i,x}, m_{i,y}, m_{i,z})^t = (\cos \phi_i \cos \theta_i, \cos \phi_i \sin \theta_i, \sin \phi_i)^t. \quad (3)$$

Thus, θ_i is the *in-plane* angle of \mathbf{m}_i with the easy axis of the hard material (measured from the positive x direction), ϕ_i the *out-of-plane* angle of \mathbf{m}_i .

2.1. Dynamics of the magnetic moment. A magnetic moment is like a spinning top, which is driven by the local effective magnetic field and subject to damping. The equation of motion for \mathbf{M}_i is the Landau–Lifshitz–Gilbert (LLG) equation,

$$\frac{\partial \mathbf{M}_i}{\partial t} = -\gamma(\mathbf{M}_i \times \mathbf{H}_i) + \frac{g}{M_i} \left(\mathbf{M}_i \times \frac{\partial \mathbf{M}_i}{\partial t} \right), \quad i \in I. \quad (4)$$

Here, \mathbf{H}_i is the effective magnetic field in the i th layer, γ the gyromagnetic constant, and g a (dimensionless) damping coefficient. Note that the LLG equation yields a magnetic moment whose magnitude is constant in time. An equivalent form of the LLG equation is

$$\frac{\partial \mathbf{M}_i}{\partial t} = -c \left[(\mathbf{M}_i \times \mathbf{H}_i) + \frac{g}{M_i} \mathbf{M}_i \times (\mathbf{M}_i \times \mathbf{H}_i) \right], \quad i \in I, \quad (5)$$

where $c = \gamma/(1 + g^2)$. We rescale t by a factor c and take $c = 1$ from here on.

The effective magnetic field is found by taking the variational derivative of the free energy,

$$\mathbf{H}_i = \mathbf{H}_a - \frac{\delta F}{\delta \mathbf{M}_i}, \quad (6)$$

where \mathbf{H}_a is the externally applied field, which we take to be uniform and constant in time. The free-energy density F is the sum of the exchange energy, the anisotropy energy, and the demagnetization energy,

$$\mathcal{F}[\mathbf{M}] = \int_{\Omega} \left[\frac{1}{2} A(z) \left| \frac{\partial \mathbf{m}}{\partial z} \right|^2 + K(z) |\mathbf{m} \times \mathbf{e}_x|^2 + \frac{1}{2} (4\pi) (\mathbf{M} \cdot \mathbf{e}_z)^2 \right]. \quad (7)$$

Here, Ω is the z interval occupied by the entire multilayered structure, A is the exchange coupling coefficient, and K is the anisotropy coefficient. The demagnetization tensor for a layer has only one element, D_{zz} ; 4π is its value for an infinitely thin flat ellipsoid [13]. In practice, one approximates \mathbf{H}_i by the expression

$$\begin{aligned} \mathbf{H}_i = & \mathbf{H}_a + \frac{1}{M_i} [J_{i,i+1}(\mathbf{m}_{i+1} - \mathbf{m}_i) - J_{i,i-1}(\mathbf{m}_i - \mathbf{m}_{i-1})] - 2 \frac{K_i}{M_i} \mathbf{e}_x \times (\mathbf{m}_i \times \mathbf{e}_x) \\ & - 4\pi M_i (\mathbf{m}_i \cdot \mathbf{e}_z) \mathbf{e}_z, \quad i \in I, \end{aligned} \quad (8)$$

where

$$\mathbf{m}_0 = \mathbf{m}_1, \mathbf{m}_{N+1} = \mathbf{m}_N. \quad (9)$$

The coupling coefficient J , which is related to A ($J = Ad^{-2}$), has the same value between layers of the same material; similarly, the anisotropy coefficient K is constant within the same material,

$$J_{i,i+1} = \begin{cases} J_h, & i = 1, \dots, N_h - 1, \\ J_{hs}, & i = N_h, \\ J_s, & i = N_h + 1, \dots, N, \end{cases} \quad K_i = \begin{cases} K_h, & i = 1, \dots, N_h, \\ K_s, & i = N_h + 1, \dots, N. \end{cases} \quad (10)$$

The actual values of these material parameters depend on the temperature; $K_s \ll K_h$ in all practical cases.

2.2. Integration of the LLG equation. The LLG equation maintains a constant magnetization, so the only quantity that changes in the course of time is the direction of the magnetic moment. We therefore begin by rewriting the LLG equation in terms of \mathbf{m} . As the equation is entirely local to each layer, we drop the index i temporarily. We use the prime $'$ to denote differentiation with respect to time.

Let H be the strength of the magnetic field, and let $\mathbf{h} = \mathbf{H}/H$ be the unit vector in the direction of \mathbf{H} ,

$$\mathbf{H}(t) = H(t)\mathbf{h}(t). \quad (11)$$

Then the LLG equation is

$$\mathbf{m}' = -H[(\mathbf{m} \times \mathbf{h}) + g\mathbf{m} \times (\mathbf{m} \times \mathbf{h})]. \quad (12)$$

We decompose the equation by means of the projection operators P and Q ,

$$Pu = (\mathbf{u} \cdot \mathbf{h})\mathbf{h}, \quad Qu = \mathbf{u} - Pu = \mathbf{h} \times (\mathbf{u} \times \mathbf{h}), \quad \mathbf{u} \in \mathbf{R}^3. \quad (13)$$

Equation (12) is equivalent to the two equations

$$P\mathbf{m}' = -HP[(\mathbf{m} \times \mathbf{h}) + g\mathbf{m} \times (\mathbf{m} \times \mathbf{h})], \quad (14)$$

$$Q\mathbf{m}' = -HQ[(\mathbf{m} \times \mathbf{h}) + g\mathbf{m} \times (\mathbf{m} \times \mathbf{h})]. \quad (15)$$

Notice the identities

$$P(\mathbf{m} \times \mathbf{h}) = \mathbf{0}, \quad P[\mathbf{m} \times (\mathbf{m} \times \mathbf{h})] = (\mathbf{m} \cdot Q\mathbf{m})\mathbf{h} = -[1 - (P\mathbf{m} \cdot P\mathbf{m})^2]\mathbf{h}, \quad (16)$$

$$Q(\mathbf{m} \times \mathbf{h}) = -JQ\mathbf{m}, \quad Q[\mathbf{m} \times (\mathbf{m} \times \mathbf{h})] = (\mathbf{m} \cdot \mathbf{h})Q\mathbf{m}, \quad (17)$$

where J is the square root of the negative identity in \mathbf{R}^2 ,

$$I = \begin{pmatrix} 1 & 0 \\ 0 & 1 \end{pmatrix}, \quad J = \begin{pmatrix} 0 & -1 \\ 1 & 0 \end{pmatrix}, \quad J^2 = -I. \quad (18)$$

Hence, we can recast Eqs. (14) and (15) in the form

$$P\mathbf{m}' = gH[1 - (P\mathbf{m} \cdot P\mathbf{m})^2]\mathbf{h}, \quad (19)$$

$$Q\mathbf{m}' = H[J - g(\mathbf{m} \cdot \mathbf{h})I]Q\mathbf{m}. \quad (20)$$

Suppose that the direction of \mathbf{H} does not change on an interval $(t, t + \Delta t)$,

$$\mathbf{h}(s) = \mathbf{h}(t), \quad s \in (t, t + \Delta t). \quad (21)$$

Then $P\mathbf{m}' = (P\mathbf{m})'$ and $Q\mathbf{m}' = (Q\mathbf{m})'$ on $(t, t + \Delta t)$, so Eqs. (19) and (20) reduce to a coupled system of differential equations for the scalar $u = (P\mathbf{m} \cdot \mathbf{h})$ in \mathbf{R} and the vector $\mathbf{v} = Q\mathbf{m}$ in \mathbf{R}^2 ,

$$u' = gH(1 - u^2) \quad \text{on } (t, t + \Delta t), \quad (22)$$

$$\mathbf{v}' = H(J - guI)\mathbf{v} \quad \text{on } (t, t + \Delta t). \quad (23)$$

From these equations we conclude that the critical states are $u = 1$, $\mathbf{v} = \mathbf{0}$ ($\mathbf{m} = \mathbf{h}$, magnetic moment parallel to the magnetic field) and $u = -1$, $\mathbf{v} = \mathbf{0}$ ($\mathbf{m} = -\mathbf{h}$, magnetic moment antiparallel to the magnetic field). The former is linearly stable, the latter unstable under infinitesimal perturbations.

We now turn to the integration of Eqs. (22) and (23). The former is independent of \mathbf{v} and can be integrated immediately. If not only the direction, but also the magnitude of H is constant on $(t, t + \Delta t)$,

$$\mathbf{H}(s) = \mathbf{H}(t), \quad s \in (t, t + \Delta t), \quad (24)$$

we find

$$u(s) = \frac{u(t) \cosh(gH(t)(s-t)) + \sinh(gH(t)(s-t))}{\cosh(gH(t)(s-t)) + u(t) \sinh(gH(t)(s-t))}, \quad s \in (t, t + \Delta t). \quad (25)$$

Next, we turn to Eq. (23). We replace the constant gH by $u'/(1-u^2)$ (from Eq. (22)) and use the identity $-uu'/(1-u^2) = (\ln(1-u^2)^{1/2})'$ to convert the equation into a differential equation for the vector $\mathbf{w} = (1-u^2)^{-1/2}\mathbf{v}$,

$$\mathbf{w}' = HJ\mathbf{w} \quad \text{on } (t, t + \Delta t). \quad (26)$$

This equation can be integrated,

$$\begin{aligned} \mathbf{w}(s) &= e^{H(t)(s-t)J} \mathbf{w}(t) \\ &= [\cos(H(t)(s-t))I + \sin(H(t)(s-t))J] \mathbf{w}(t), \quad s \in (t, t + \Delta t). \end{aligned} \quad (27)$$

From the expression (25) we obtain

$$(1-u(s)^2)^{1/2} = \frac{(1-u(t)^2)^{1/2}}{\cosh(gH(t)(s-t)) + u(t) \sinh(gH(t)(s-t))}, \quad (28)$$

so

$$\mathbf{v}(s) = \frac{\cos(H(t)(s-t))I + \sin(H(t)(s-t))J}{\cosh(gH(t)(s-t)) + u(t) \sinh(gH(t)(s-t))} \mathbf{v}(t), \quad s \in (t, t + \Delta t). \quad (29)$$

These results suggest the following choice of the integration scheme for Eq. (12):

$$\begin{aligned} \mathbf{m}_{n+1} &= \frac{(\mathbf{m}_n \cdot \mathbf{h}_n) \cosh(gH_n \Delta t) + \sinh(gH_n \Delta t)}{\cosh(gH_n \Delta t) + (\mathbf{m}_n \cdot \mathbf{h}_n) \sinh(gH_n \Delta t)} \mathbf{h}_n \\ &\quad + \frac{\cos(H_n \Delta t)I + \sin(H_n \Delta t)J}{\cosh(gH_n \Delta t) + (\mathbf{m}_n \cdot \mathbf{h}_n) \sinh(gH_n \Delta t)} \mathbf{h}_n \times (\mathbf{m}_n \times \mathbf{h}_n), \end{aligned} \quad (30)$$

where $\mathbf{m}_{n+1} = \mathbf{m}(t_{n+1})$, $\mathbf{m}_n = \mathbf{m}(t_n)$, $\mathbf{h}_n = \mathbf{h}(t_n)$, $H_n = H(t_n)$, and $\Delta t = t_{n+1} - t_n$.

The algorithm (30) is unconditionally stable for all values of Δt . Of course, the quality of the approximation suffers as Δt increases. However, the algorithm explicitly displays the relationship between the size of Δt and the local error in the time integration. The rate of precession of \mathbf{m} around the polar axis is governed by H , the magnitude of the local effective field: in one time step, \mathbf{m} precesses through an angle $H\Delta t$. Therefore, by properly choosing Δt , we can resolve the fastest precessional motion in a given number of time steps per period. Since H varies over the course of a simulation, we have a natural and direct means to adjust the size of Δt to the current dynamical state, while maintaining the resolution of the precessional motion.

Other algorithms for the numerical integration of the LLG equation have been proposed recently by Nigam [14] and E and Wang [15].

2.3. Computing equilibrium configurations. The analysis in the preceding section suggests the following algorithm for finding equilibrium spin configurations. Starting from a given equilibrium state $\mathbf{M} = \{\mathbf{M}_i : i \in I\}$ at time t_0 , one uses Eq. (8) to compute the magnetic field \mathbf{H}_i in each layer at t_0 . Having found $\mathbf{H}_i(t_0)$ for all $i \in I$, one advances in time to $t_1 = t_0 + \Delta t$ and uses Eqs. (2) and (30) to compute \mathbf{M} at t_1 . If Δt is sufficiently small, $\mathbf{M}(t_1)$ is a close approximation of the state of the system at time t_1 . One continues this process, finding approximations at successive times $t_n = t_0 + n\Delta t$, $n = 1, 2, \dots$, until equilibrium is reached.

3. Numerical results. The algorithm of the preceding section has been used to study hysteresis phenomena in hard/soft bilayers that are driven by an applied field \mathbf{H}_a that is uniform, constant in time, and parallel to the planes of the atomic layers. The expression for the effective magnetic field, Eq. (8), decomposes into an in-plane component,

$$\begin{aligned} \mathbf{H}_i \times \mathbf{e}_z = \mathbf{H}_a \times \mathbf{e}_z + \frac{1}{M_i} [J_{i,i+1}(\mathbf{m}_{i+1} - \mathbf{m}_i) - J_{i,i-1}(\mathbf{m}_i - \mathbf{m}_{i-1})] \times \mathbf{e}_z \\ - 2 \frac{K_i}{M_i} (\mathbf{m}_i \cdot \mathbf{e}_y) \mathbf{e}_x, \quad i \in I, \end{aligned} \quad (31)$$

and an out-of-plane component,

$$\begin{aligned} \mathbf{H}_i \cdot \mathbf{e}_z = \frac{1}{M_i} [J_{i,i+1}(\mathbf{m}_{i+1} - \mathbf{m}_i) - J_{i,i-1}(\mathbf{m}_i - \mathbf{m}_{i-1})] \cdot \mathbf{e}_z \\ - 2 \frac{K_i}{M_i} \mathbf{m}_i \cdot \mathbf{e}_z - 4\pi M_i \mathbf{m}_i \cdot \mathbf{e}_z, \quad i \in I. \end{aligned} \quad (32)$$

When the system is in an equilibrium state, the effective magnetic field is parallel (or antiparallel) to the magnetic spin; see Section 2.2. Hence, each \mathbf{H}_i is a multiple of \mathbf{m}_i , and Eq. (32) reduces to a homogeneous system of linear algebraic equations for the set of scalars $\{\mathbf{m}_i \cdot \mathbf{e}_z : i \in I\}$. In general, this system admits only the trivial solution, so the magnetic moments lie in the plane of the atomic layers. In the notation of Eq. (3), $\phi_i = 0$ for all $i \in I$ at equilibrium, and the only relevant variables are the in-plane angles $\{\theta_i : i \in I\}$. (Of course, the magnetic spin may have an out-of-plane component during the transient phase of the computation.)

In the numerical simulations we focus on the in-plane angle of the magnetic spin at equilibrium and investigate its behavior as a function of the strength H_a and the direction θ_a of the applied field,

$$\mathbf{H}_a = H_a \mathbf{h}_a, \quad \mathbf{h}_a = (\cos \theta_a, \sin \theta_a, 0)^t. \quad (33)$$

The following computations refer to a bilayer configuration consisting of $N_h = 115$ atomic layers of Sm-Co (a hard material) and $N_s = 100$ atomic layers of Fe (a soft material). A different configuration is used in Section 3.3, where we make a comparison with some magneto-optical measurements. Table 1 gives the values of the material parameters A , K , and M , as well as the values of the coupling coefficient J ($J = Ad^{-2}$, $d = 2 \text{ \AA}$). In all cases, the damping coefficient $g = 0.5$.

TABLE 1. Numerical values of the parameters.

	A (erg/cm)	J (erg/cm ³)	K (erg/cm ³)	M (emu/cm ³)
Fe	$2.8 \cdot 10^{-6}$	$7.0 \cdot 10^9$	$1.0 \cdot 10^3$	1,700
Interface	$1.8 \cdot 10^{-6}$	$4.5 \cdot 10^9$	—	—
Sm-Co	$1.2 \cdot 10^{-6}$	$3.0 \cdot 10^9$	$5.0 \cdot 10^7$	550

3.1. Rotational hysteresis. The case $H_a = 4800$ oersteds is typical, at least for moderate values of H_a (see Section 3.2).

The simulations show that the equilibrium spin configurations for increasing θ_a ($0 < \theta_a < 2\pi$) and decreasing θ_a ($2\pi > \theta_a > 0$) are mirror images of each other. Figure 1 shows two sets of magnetic spin configurations at equilibrium for various values of θ_a , one set (left) as θ_a increases from 0 to 2π , the other set (right) as θ_a decreases from 2π to 0. The heavy dots represent the endpoints of the magnetic spin (a unit vector) in each layer for various angles θ_a ; the values of θ_a , in degrees, are indicated near the top layer. (The dots merge into a solid line where the magnetic spins in adjacent layers are close.)

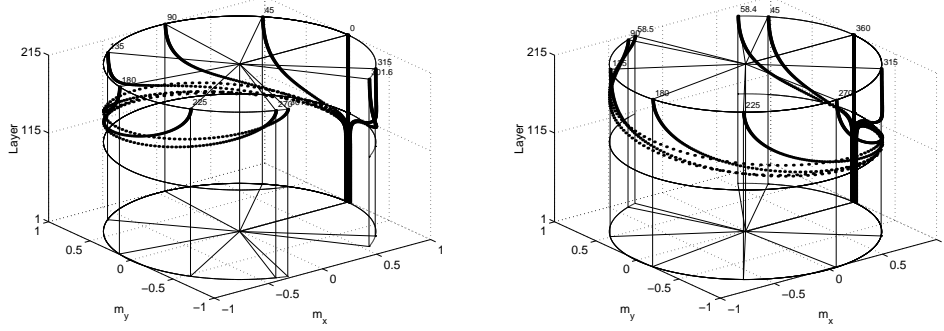


FIGURE 1. Equilibrium spin configurations; $H_a = 4800$ oersteds. Left: θ_a increasing, right: θ_a decreasing.

Notice that the chirality (“handedness”) of the chain of magnetic spins changes from positive at $\theta_a = 301.5$ to negative at $\theta_a = 301.6$ degrees and from negative at $\theta_a = 58.5$ to positive at $\theta_a = 58.4$ degrees. Figure 2 shows this change in a different way.

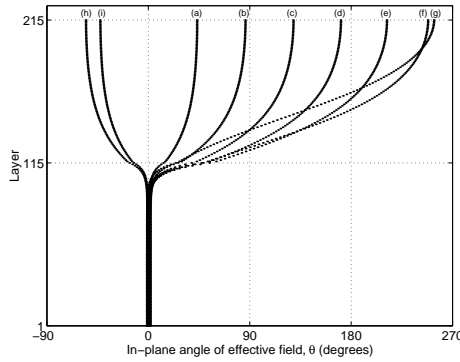


FIGURE 2. In-plane angle θ_i vs. i ; $H_a = 4800$ oersteds; (a) $\theta_a = 45$, (b) $\theta_a = 90$, (c) $\theta_a = 135$, (d) $\theta_a = 180$, (e) $\theta_a = 225$, (f) $\theta_a = 270$, (g) $\theta_a = 301.5$, (h) $\theta_a = 301.6$, (i) $\theta_a = 315$ degrees.

Here, we have plotted the in-plane angle θ_i against the layer index i for increasing values of θ_a . (The graphs for decreasing values of θ_a are obtained by symmetry.) First, the graph changes continuously (but not monotonically) as θ_a increases from

0 to 301.5 degrees, θ_i increasing with i (positive chirality). Then it changes discontinuously as θ_a increases to 301.6 degrees: θ_i suddenly becomes decreasing instead of increasing with i . Finally, it changes continuously again as θ_a increases further, θ_i decreasing with i (negative chirality), to return to the original graph ($\theta_i = 0$ for all $i \in I$) as θ_a reaches 360 degrees. In all cases, the spin is fixed along the easy axis ($\theta_i = 0$) in most of the hard layers; it begins to deviate from the easy axis only as one approaches the interface ($i = 115$). The first derivative is discontinuous at the interface, and the tangent is vertical in the top layer ($i = 215$).

The change in chirality is irreversible and induces *rotational hysteresis*. The in-plane angle of each spin vector traverses a different trajectory as the applied field rotates 360 degrees in the forward and backward direction. The hysteresis loop has the same shape, and particularly the same width, in all layers. Its vertical dimension contracts gradually as one descends through the soft layers, to disappear entirely in the hard layers somewhat below the interface; see Fig. 3.

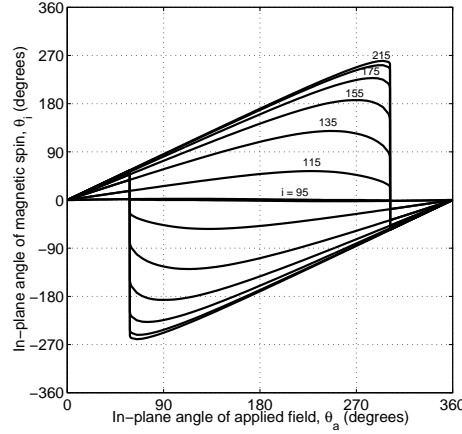
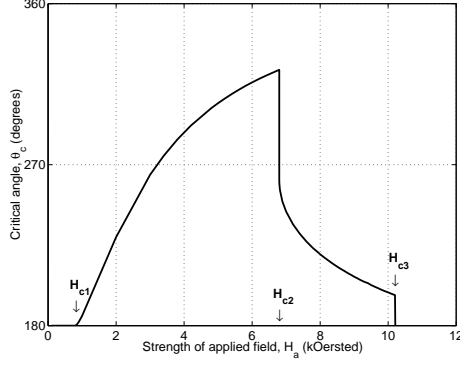


FIGURE 3. Rotational hysteresis: in-plane angle θ_i vs. θ_a ; $H_a = 4800$ oersteds; $i = 95, 115, 135, 155, 175, 195, 215$.

3.2. Two types of rotational hysteresis. When the strength of the applied field is varied, we observe different modes of irreversible behavior. We recall (Fig. 3) that, as θ_a increases from 0, the chirality changes discontinuously from positive to negative as the direction of the applied field deviates sufficiently from the easy axis. We denote the critical value of the angle θ_a by θ_c ($\theta_c = 301.5\dots$ at $H_a = 4800$ oersteds). Figure 4 shows the variation of θ_c with H_a .

As long as H_a is sufficiently small, the magnetization process is reversible. At a first critical value of H_a , marked H_{c1} , the chirality of the chain of magnetic spins changes for the first time, and rotational hysteresis of the type discussed in the preceding section (with a basic period of 360 degrees) sets in. The width of the hysteresis loop, which is symmetric around $\theta_a = \pi$, increases monotonically from 0 at $H_a = H_{c1}$ to some value less than 2π .

At a second critical value of H_a , marked H_{c2} , a sharp discontinuity occurs. The hysteresis loop narrows significantly and continues to narrow as H_a increases beyond H_{c2} . The cause of this discontinuity becomes obvious in Fig. 5, where we have plotted θ_i against i ; cf. Fig. 2. (The bottom 80 layers of hard material, where θ_i does not deviate noticeably from 0, are not included in this figure.) As H_a

FIGURE 4. The critical angle θ_c as a function of H_a .

reaches the value H_{c2} , the chain of spins has been stretched to its widest extent; it can no longer support the span in the top layer, stiffens suddenly, and becomes more like a rigid rod. The rod-like behavior is apparent from the increasing range where the chain is almost vertical.

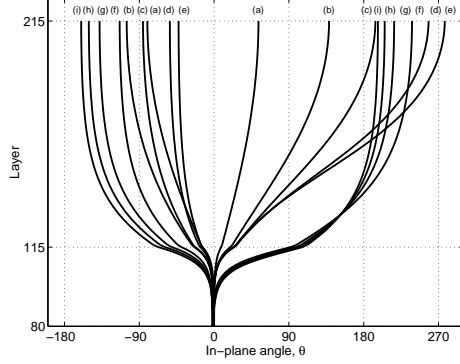


FIGURE 5. In-plane angle θ_i vs. i ; (a) $H_a = 1000$, (b) $H_a = 2000$, (c) $H_a = 3000$, (d) $H_a = 5000$, (e) $H_a = 6000$, (f) $H_a = 7000$, (g) $H_a = 8000$, (h) $H_a = 9000$, (i) $H_a = 10,000$ oersteds. Right branches: θ_a just below θ_c , left branches: θ_a just above θ_c .

The structural change in the chain of spins has some of the characteristics of a phase transition. For example, we observe a significant increase in the equilibration time (by two orders of magnitude) as θ_a approaches θ_c ; see Fig. 6. Also, the increasing size of the rigid domain near H_{c2} is reminiscent of a diverging correlation length.

At a third critical value of H_a , marked H_{c3} , another significant change occurs. The field has now become sufficiently strong to move the spins in both the soft and the hard materials. From here on, the chain of spin vectors changes over its entire length, maintaining its chirality. Figure 7 gives θ_i vs. i for increasing values of θ_a . (The graphs for decreasing values of θ_a are obtained by symmetry.) The value $H_a = 10,400$ oersteds is just above H_{c3} . This figure should be compared with Fig. 2 for the standard case, $H_a = 4800$ oersteds. The exact determination of H_{c3} is delicate; in our numerical simulations we found a slight rate dependence in the regime near H_{c3} .

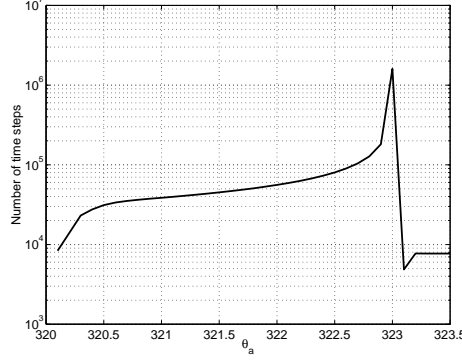


FIGURE 6. Equilibration time near θ_c ; $H_a = 6797$ oersteds, $\theta_c = 323.0$ degrees.

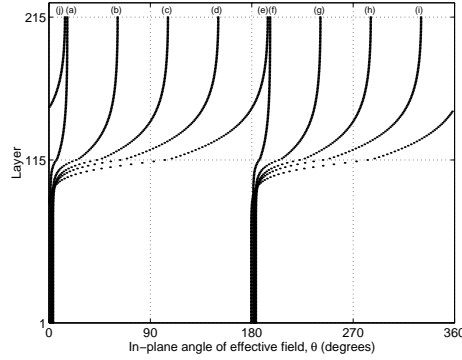


FIGURE 7. In-plane angle θ_i vs. i ; $H_a = 10,400$ oersteds; (a) $\theta_a = 16$, (b) $\theta_a = 61$, (c) $\theta_a = 106$, (d) $\theta_a = 151$, (e) $\theta_a = 195$, (f) $\theta_a = 196$, (g) $\theta_a = 241$, (h) $\theta_a = 286$, (i) $\theta_a = 331$, (j) $\theta_a = 375$ degrees.

Because the chain of spins behaves more like an elastic spring than a stiff rod, a new type of rotational hysteresis emerges, whose basic period can be any multiple of 180 degrees. Figure 8 shows three graphs: one graph (c) is along the diagonal; the other two (a and b) are symmetric with respect to the diagonal. The outer graph (a) shows θ_i for $i = 85$ (hard layer). The part below the diagonal is traversed in the upward direction as θ_a increases from 0; the part above the diagonal is traversed in the downward direction as θ_a decreases from 360 degrees. The spin is oriented in either the positive or the negative x direction. Transitions occur at θ_c and at every multiple of π beyond θ_c . The center graph (c) shows θ_i for $i = 215$ (top layer). The orientation of this spin varies continuously with θ_a and is perfectly reversible. Finally, the middle graph (b) shows θ_i for $i = 115$ (at the interface). Here, the spin rotates continuously until it jumps. The jumps occur at θ_c and at every multiple of π beyond θ_c . The graphs for the remaining layers fill the space between the ones drawn in the figure. The main point to observe is that the graphs for θ_a increasing always increase and stay below the diagonal, while those for θ_a decreasing always decrease and stay above the diagonal. Hence, chirality is preserved in both cases.

When the direction of θ_a is reversed, θ_i crosses the diagonal as soon as $\theta_a - \theta_c$ is a multiple of π ; after crossing, it remains on the part of the graph situated on the

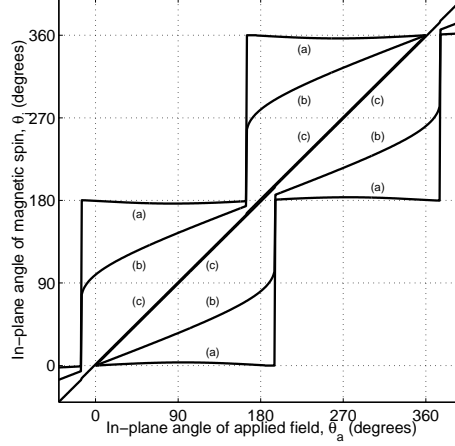


FIGURE 8. In-plane angle θ_i vs. θ_a ; $H_a = 10,400$ oersteds; (a) $i = 85$, (b) $i = 115$, (c) $i = 215$.

newly reached side of the diagonal. Because there is a gap between the graphs for θ_i in the interior layers and the diagonal, the orientation of the magnetic spin shows rotational hysteresis in all interior layers. This hysteresis is caused by a full-length transition of the chain of magnetic spins, rather than the partial-range transition that was responsible for the hysteresis below H_{c3} .

3.3. Comparison with experiment. Quantities such as the magnetic moment are fundamental to describe the state of the system, but they are not directly measurable in an experiment. Measurable quantities are the *torque density* T and the *magnetization angle* α ,

$$T = H_a d \sum_{i \in I} M_i \sin(\theta_a - \theta_i), \quad \alpha = \tan^{-1} \frac{\sum_{i \in I} M_i \sin \theta_i}{\sum_{i \in I} M_i \cos \theta_i}. \quad (34)$$

Both T and α reflect the hysteretic behavior of the magnetic moments. Figure 9 shows the torque density computed at $H_a = 4800$ and $10,400$ oersteds.

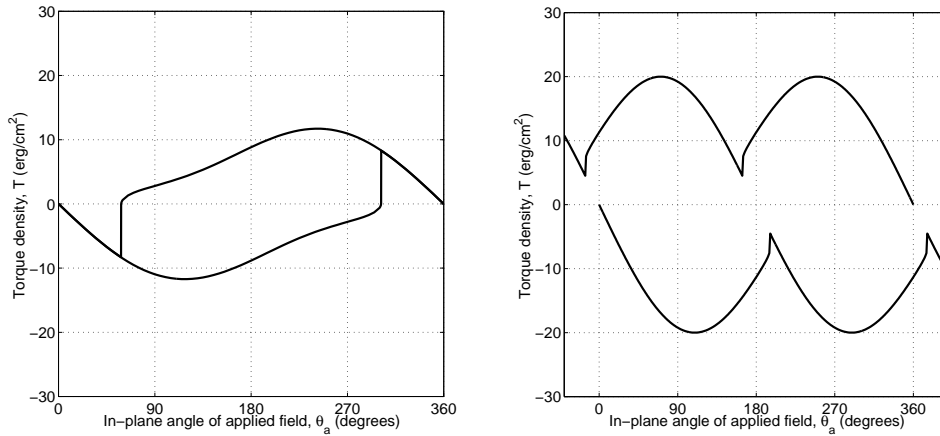


FIGURE 9. Torque density; $H_a = 4800$ (left) and $10,400$ (right) oersteds.

Experimental torque measurements at comparable values of H_a show similarly shaped graphs, with extrema at approximately the same values of θ_a , but significantly narrower hysteresis loops [10].

In Fig. 10, we compare results for the magnetization angle with experimental data. The data were obtained by magneto-optical means for a bilayer consisting of $N_h = 100$ atomic layers of Sm-Co and $N_s = 250$ atomic layers of Fe; the simulation curves also refer to this configuration [11]. The measurements were done at relatively low fields ($H_a = 360, 600$, and 840 oersteds) and for a limited range of directions ($\theta_a = 0 : 10 : 230$ degrees).

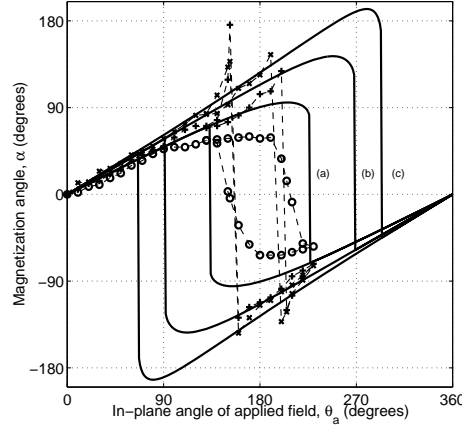


FIGURE 10. Magnetization angle; (a) $H_a = 360$ (o), (b) $H_a = 600$ (+), and (c) $H_a = 840$ (\times) oersteds.

There is certainly qualitative agreement, but the simulations generally yield wider hysteresis loops than the experiments, and the discrepancy becomes greater as the field strength increases. This behavior can be explained by the fact that the model used in the simulations is a single-domain model, which does not allow for the important phenomenon of nucleation and motion of nanodomains. As a result, the demagnetization energy is seriously overestimated. In realistic simulations, one must use multidimensional models and allow for lateral inhomogeneities [11].

4. Conclusions. In this article we have addressed an important issue in micro-magnetics: magnetization reversal in layered spring magnets. We have used a one-dimensional model of a film consisting of atomic layers of a soft material on top of atomic layers of a hard material with strong coupling at the interface, assuming no variation in the lateral directions. The state of such a system is described by a chain of magnetic spin vectors. Each spin vector behaves like a spinning top driven by the local magnetic field and subject to damping. The dynamics are described by a system of LLG equations, Eq. (5), coupled with a variational equation for the magnetic field, Eq. (8).

We have presented an integration procedure that maintains the invariance of the magnetization (the magnitude of the magnetization vector) and proposed an algorithm for finding the equilibrium state of the system.

We have applied the algorithm to simulate magnetization reversal in layered spring magnets. The results show that a layered spring magnet exhibits rotational hysteresis with a basic period of 360 degrees at moderately strong fields and rotational hysteresis with a basic period of 180 degrees at strong fields. The former type of hysteresis is induced by a partial-length transition of the chain of magnetic spins; the transition occurs only in the soft material and causes a change of chirality. The hysteresis in strong fields is induced by a full-length transition of the chain of spins in both the hard and the soft layers; it is much weaker than the rotational hysteresis at moderately strong fields and can cover any period that is a multiple of the basic period.

The numerical results for the torque and magnetization angle agree qualitatively with the experimental data but differ at the quantitative level. In particular, the one-dimensional model seriously overestimates the demagnetization energy, since it does not allow for the nucleation and motion of nanodomains. In realistic simulations, lateral inhomogeneities must be taken into account.

Acknowledgments. This work was supported by the Mathematical, Information, and Computational Sciences Division subprogram of the Office of Advanced Scientific Computing Research, U.S. Department of Energy, under Contract W-31-109-Eng-38. Most of the numerical simulations were carried out by Jaime Hernandez Jr. (University of Texas at El Paso), who was a participant in the Energy Research Undergraduate Laboratory Fellowship program at Argonne National Laboratory (summer 2000).

REFERENCES

- [1] E. F. Kneller and R. Hawig, THE EXCHANGE-SPRING MAGNET: A NEW MATERIAL PRINCIPLE FOR PERMANENT MAGNETS, *IEEE Trans. Mag.*, **27** (1991), 3588–3600.
- [2] J. M. D. Coey and R. Skomski, NEW MAGNETS FROM INTERSTITIAL INTERMETALLICS, *Physica Scripta*, **T49** (1993), 315–321.
- [3] R. Skomski and J. M. D. Coey, GIANT ENERGY PRODUCT IN NANOSTRUCTURED TWO-PHASE MAGNETS, *Phys. Rev. B*, **48** (1993), 15812–15816.
- [4] R. Fischer, T. Leinewebber, and H. Kronmüller, FUNDAMENTAL MAGNETIZATION PROCESSES IN NANOSCALED COMPOSITE PERMANENT MAGNETS, *Phys. Rev. B*, **57** (1998), 10723–10732.
- [5] E. E. Fullerton, J. S. Jiang, C. H. Sowers, J. E. Pearson, and S. D. Bader, STRUCTURE AND MAGNETIC PROPERTIES OF EXCHANGE-SPRING SM-CO/CO SUPERLATTICES, *Appl. Phys. Lett.*, **72**, 380–382 (1998).
- [6] J. S. Jiang, E. E. Fullerton, C. H. Sowers, A. Inomata, S. D. Bader, A. J. Shapiro, R. D. Shull, V. S. Gornakov, and V. I. Nikitenko, “Spring magnet films,” *IEEE Trans. Magn.*, **35** (2000), 3229–3234.
- [7] L. Landau and E. Lifshitz, ON THE THEORY OF MAGNETIC PERMEABILITY IN FERROMAGNETIC BODIES, *Physik. Z. Soviet Union*, **8** (1935), 153–169.
- [8] T. L. Gilbert, A LAGRANGIAN FORMULATION OF GYROMAGNETIC EQUATION OF THE MAGNETIZATION FIELD, *Phys. Rev.*, **100** (1955), 1243.
- [9] J. Fidler and T. Schrefl, MICROMAGNETIC MODELING—THE CURRENT STATE OF THE ART, *J. Phys. D: Appl. Phys.*, **33** (2000), R135–R156.
- [10] S. David, S. S. P. Parkin, E. E. Fullerton, C. Platt, A. Berkowitz, J. S. Jiang, and S. D. Bader, FIELD DEPENDENT REVERSAL MODES IN EXCHANGE-SPRING THIN FILMS FROM ROTATIONAL HYSTERESIS ANALYSIS, *J. Appl. Phys.* (to appear).
- [11] R. D. Shull, A. J. Shapiro, V. S. Gornakov, V. I. Nikitenko, J. S. Jiang, H. G. Kaper, G. K. Leaf, and S. D. Bader, SPIN SPRING BEHAVIOR IN EXCHANGE COUPLED SOFT AND HIGH-COERCIVITY HARD FERROMAGNETS, *J. Appl. Phys.* (to appear).
- [12] J. S. Jiang, H. G. Kaper, and G. K. Leaf, NUMERICAL SIMULATIONS OF MAGNETIC REVERSAL IN LAYERED SPRING MAGNETS, ANL/MCS-TM-247, Argonne National Laboratory; January 2001.
- [13] H. N. Bertram, “Theory of magnetic recording,” Cambridge University Press, 1994.

- [14] N. Nigam, EFFICIENT MICROMAGNETIC CALCULATIONS, Third SIAM Conf. on Mathematical Aspects of Materials Science, Philadelphia, Pennsylvania; May 2000.
- [15] Weinan E and X. P. Wang, NUMERICAL METHODS FOR THE LANDAU–LIFSHITZ EQUATION, SIAM J. Numer. Anal. (to appear).

Received January 2001.

E-mail address: `jiang@anl.gov`

E-mail address: `kaper@mcs.anl.gov`

E-mail address: `leaf@mcs.anl.gov`